Impact of eddy-wind interaction on eddy demographics and phytoplankton community structure in a model of the North Atlantic Ocean

Laurence A. Anderson[a*], Dennis J. McGillicuddy, Jr.[a], Mathew E. Maltrud[b], Ivan D. Lima[c], Scott C. Doney[c]

[a]Department of Applied Ocean Physics and Engineering, Woods Hole Oceanographic Institution, Woods Hole, Massachusetts, USA
[b]Fluid Dynamics Group, Theoretical Division, Los Alamos National Laboratory, Los Alamos, New Mexico, USA
[c]Department of Marine Chemistry and Geochemistry, Woods Hole Oceanographic Institution, Woods Hole, Massachusetts, USA

[*]Corresponding author. tel: +1 508 289 3742; fax: +1 508 457 2194; e-mail: landerson@whoi.edu; post: Laurence Anderson, WHOI – MS #9, Woods Hole, MA 02543, USA.

Abstract

Two eddy-resolving (0.1-degree) physical-biological simulations of the North Atlantic Ocean are compared, one with the surface momentum flux computed only from wind velocities and the other using the difference between air and ocean velocity vectors. This difference in forcing has a significant impact on the intensities and relative number of different types of mesoscale eddies in the Sargasso Sea. Eddy/wind interaction significantly reduces eddy intensities and increases the number of mode-water eddies and "thinnies" relative to regular cyclones and anticyclones; it also modifies upward isopycnal displacements at the base of the euphotic zone, increasing them in the centers of mode water eddies and at the edges of cyclones, and decreasing them in the centers of cyclones. These physical changes increase phytoplankton growth rates and biomass in mode-water eddies, bringing the biological simulation into better agreement with field data. These results indicate the importance of including the eddy/wind interaction in simulations of the physics and biology of eddies in the subtropical North Atlantic. However, eddy intensities in the simulation with eddy/wind interaction are lower than observed, which suggests a decrease in horizontal viscosity or an increase in horizontal grid resolution will be necessary to regain the observed level of eddy activity.

Keywords: mesoscale eddies, phytoplankton, community composition, air-sea interaction, wind stress, Ekman pumping, 25-30 °N 58-68 °W

1. Introduction

Recent field observations in the Sargasso Sea exhibit relationships between different phytoplankton groups and different types of mesoscale eddies. Enhanced diatom and dinoflagellate biomass has been found in mode-water eddies (Sweeney et al., 2003; McGillicuddy et al., 2007; Benitez-Nelson and McGillicuddy, 2008; Mourino-Carballido, 2009; Krause et al., 2010). Enhanced *Prochlorococcus* and *Synechococcus* biomass has been observed in cyclones (Sweeney et al., 2003; Mourino-Carballido, 2009). Enhanced biomass of nitrogen-fixing *Trichodesmium* spp. has been found associated with anticyclones (Davis and McGillicuddy, 2006). Unfortunately in most cases the data are insufficient to determine whether these relationships are due to *in situ* growth, horizontal advection across large-scale gradients, or local aggregation.

Intensive field observations in the Sargasso Sea in 2005 found persistent upwelling at 100 meters depth at the core of an anticyclonic mode-water eddy (Ledwell et al., 2008). This was attributed to a surface divergence caused by variations in wind stress across the eddy. The air-to-sea momentum flux is smaller on the side of an eddy where wind and currents are in the same direction, compared to the other side where wind and currents are in opposite directions. This generates a divergence in the horizontal Ekman transport at the center of an anticyclone (and convergence in a cyclone) regardless of wind direction, driving vertical velocities at the base of the Ekman layer which can penetrate to the main thermocline at the center of eddies (Dewar and Flierl, 1987; Martin and Richards, 2001). For brevity this will be referred to as “eddy/wind interaction”.

Eddy/wind interaction was apparently the driver behind the increased diatom biomass and primary productivity found within the eddy (McGillicuddy et al., 2007).

Until recently, most eddy-resolving models have used surface momentum fluxes computed from wind velocities alone, and thus do not include the impact of eddy/wind interaction on vertical velocities and eddy characteristics. Recent simulations show that including eddy/wind interaction significantly decreased the amount of energy in the mesoscale eddy field (Zhai and Greatbatch, 2007; Xu and Scott, 2008; Small et al., 2009). Eden and Dietze (2009) found that including the eddy/wind interaction caused a 10-50% reduction in eddy activity though only a 5% reduction in new production.

Here we compare the results of two eddy-resolving physical-biological simulations of the North Atlantic Ocean, one of which computes the surface momentum flux only from wind velocity vectors, and the other using air-minus-ocean velocity vectors. First we describe differences in the mean physical structure of mesoscale eddies in the two cases. We then examine how these physical differences impact the relationships between eddy type and simulated phytoplankton species composition. We concentrate on the Sargasso Sea, where data for comparison are relatively abundant. However, even in this relatively data-rich area, the number of synoptic realizations of mesoscale biological and biogeochemical distributions is insufficient to deduce reliable statistics that can be compared directly with the model. We therefore focus our model-data comparisons on qualitative aspects, such as whether or not the model is able to simulate the distinct biological responses to each of the various types of eddies.

2. Methods

The coupled physical-biogeochemical model is based on the Los Alamos Parallel Ocean Program (Smith et al., 1992; 2000). It was configured for the North Atlantic (20 °S to 72 °N) using an "eddy-resolving" horizontal grid resolution of 11.1 cos ϕ km, where ϕ is latitude. The primary differences between these runs using POP 2.0.1 and the POP 1.1.1 simulations described in McGillicuddy et al. (2003) are as follows. The number of time steps per day was increased from 150 to 200 for sufficient numerical precision of the biological model. The number of vertical levels was increased from 40 to 42 (viz. the maximum depth increased from 5500 m to 6000 m). Partial bottom cells were included to better simulate the interaction of currents with bathymetry. Vertical mixing was switched from explicit-in-time with convective adjustment to implicit-in-time, and from Richardson number dependent (Pacanowski and Philander, 1981) to KPP (Large et al., 1994). Horizontal viscosity was changed from biharmonic only (-27e+9 m^4 s^{-1}) to biharmonic plus Laplacian (-6.75e+9 m^4 s^{-1} and 35.5 m^2 s^{-1}; Hecht et al., 2008). The air-sea drag coefficient was changed from wind-speed dependent only (Large and Pond, 1981) to air-sea stability dependent (Large and Pond, 1982). The heat forcing was changed from a shortwave flux plus restoring to monthly SST climatology (Barnier et al., 1995) to heat fluxes computed from bulk formulae using NCEP atmospheric variables (air temperature, humidity, wind speed, shortwave and downward longwave flux) and model SST. Surface salinity forcing was changed from restoring to monthly salinity climatology to monthly precipitation climatology plus evaporation based on the latent heat flux. The model forcing was changed to a 6-hourly, repeating "normal-year" atmospheric forcing (Large and Yeager, 2004), so that the interannual variability in the

112 circulation would be due solely to dynamic adjustment and not due to interannual
113 variability in the forcing.
114 A 24-box biogeochemical-ecosystem model (BEC; Moore and Doney, 2007;
115 Moore et al., 2004, 2006) was incorporated into the physical model. This model includes
116 three phytoplankton groups: diatoms (DIAT), small phytoplankton (SP) and N_2-fixing
117 diazotrophs (DIAZ, representing *Trichodesmium* spp.). As such, it can be tested directly
118 with the observed relationships between eddies and phytoplankton species composition
119 mentioned in Sec. 1. The limiting nutrients are PO_4, NO_3, NH_4, Fe and SiO_3 (for
120 diatoms). The MPDCD advection scheme was used for biological tracers (Oschlies and
121 Garcon, 1999), which is a centered-difference advection scheme with a flux limiter to
122 prevent negative tracer values.
123 BEC model parameters were mostly the same as in Moore and Doney (2007),
124 although several parameters were tuned to improve agreement with observations in the
125 North Atlantic. This was accomplished by simultaneously optimizing with data (NO_3,
126 PO_4, Chl, HPLC-estimated diatom Chl, primary production and sinking POC flux) from
127 the Bermuda Atlantic Time Series (BATS; Steinberg et al., 2001) at 32 °N 64 °W and
128 North Atlantic Bloom Experiment (NABE; Ducklow and Harris, 1993) at 47 °N 20 °W
129 using the Regional Testbed model (Friedrichs et al., 2007). The biological model
130 parameter changes included the following: reducing the diatom mortality threshold
131 (*loss_thres_diat* from 0.01 to 0.001 μM C) to lower diatom biomass in the subtropical
132 gyre but not in high latitudes; increasing the small phytoplankton and diatom PO_4 uptake
133 half-saturation coefficients (*sp_kPO4* from 0.0003125 to 0.005 μM, *diat_kPO4* from
134 0.005 to 0.02 μM) both to increase surface PO_4 toward observed values, which

consequently improved the diazotroph vertical distribution; and increasing the diatom and small phytoplankton maximum growth rate at 30 °C (*PCref* from 3.0 to 3.6 d^{-1}) and increasing the zooplankton grazing half-saturation constant (*z_grz* from 1.05 to 1.35 μM C), which increase total Chl and primary production.

The coupled physical-biological simulation was initialized with World Ocean Atlas 2001 January temperature, salinity and nutrients (Stephens et al., 2002; Boyer et al., 2002; Locarnini et al., 2002; Conkright et al., 2002), GLODAP climatology dissolved inorganic carbon and alkalinity (Key et al., 2004) and the other biological state variables with year 800 results of a coarse-resolution global simulation. This simulation was run for 14.5 years until quasi-equilibrium. The changes to the biological model parameter values mentioned in the preceding paragraph were then made, the nutrients (NO_3, PO_4, SiO_3 and O_2) re-initialized with World Ocean Atlas 2005 July distributions (Garcia et al., 2006a,b), and the coupled model run for 7 more years. Basin-averaged kinetic energy shows short-term temporal variability, but appears to be in quasi-equilibrium in the last 7 years of simulation (Figure 1a of the online Supplementary Material). The biological fields reached quasi-equilibrium after approximately 3 years of spin-up (Supplementary Figure 1b), in part due to the fact that semi-labile dissolved organic carbon, nitrogen and phosphorus were not starting from constant values but from near-equilibrium large-scale distributions.

Model output was saved as 5-day averages. Large-scale spatial trends were computed from each 5-day average by spatially smoothing with a Gaussian filter with a 3° (30 grid point) e-folding scale and a 7.5° maximum radius. The difference between each 5-day average and its large-scale spatial trend was used to estimate the mesoscale

anomaly field. Although the model solution clearly contains submesoscale variability, it is underrepresented at this grid resolution (Levy et al., 2001). For eddy locating purposes only, further smoothing of sea level anomaly and density with a 0.4° e-folding scale Gaussian filter (maximum radius 1.0°) was used to filter out submesoscale structure. To be approximately consistent with the location of the BATS data and EDDIES field observations, model output is examined in a Sargasso subdomain between 25-30 °N and 58-68 °W for year days 150-275 of the last 4 years of the simulation. The observations extend to 32 °N, but the domain is shifted 2° south to avoid the strong influence of Gulf Stream rings on the analysis.

3. Results

The simulation that uses the surface momentum flux computed only from wind velocities will be referred to as "Run 1" (no eddy/wind interaction), and the simulation that uses the difference between air and ocean velocities will be referred to as "Run 2" (with eddy/wind interaction).

Eddies were identified as extrema in mesoscale sea level anomaly (SLA), and classified as one of four types: regular cyclone ("C"; negative SLA and positive density anomaly at 97 m), regular anticyclone ("A"; positive SLA and negative density anomaly at 97 m), mode-water eddy ("M"; positive SLA and positive density anomaly) and "thinny" ("T"; negative SLA and negative density anomaly). The name "thinny" derives from the fact that in the Sargasso these eddies have a relatively "thin" layer of 18-degree Mode Water between 100 m and the main thermocline at 700 m, while "mode-water"

181 eddies have a relatively thick layer. In both cases, displacement of the main thermocline
182 dominates geostrophic velocities and SLAs, such that thinnies are cyclonic and mode-
183 water eddies are anticyclonic. The density anomaly at 97 m is of particular interest
184 because in the Sargasso it is the approximate depth of the nitracline, the deep chlorophyll
185 maximum, and the base of the euphotic zone. Isopycnal displacements at this depth are
186 thus expected to induce a biological response (McGillicuddy et al., 1999). This
187 classification method can be misleading when and where mixed-layer depth exceeds 97
188 m (i.e. in winter), and thus we restrict our period of analysis accordingly.

189 Mean vertical transects of various properties through each type of eddy for Run 2
190 (with eddy-wind interaction) are given in online Supplementary Figures 2-7. As the eddy-
191 induced horizontal gradients in all properties of interest are small compared with vertical
192 gradients, background profiles were removed to reveal the anomaly fields, which indicate
193 the modulation the eddies cause to the mean. These anomaly transects (also given in
194 online Supplementary Figures 2-7) show different responses in the euphotic zone and the
195 aphotic zone, typically divided at 104 m (which is the bottom interface of the model grid
196 box centered at 97 m). Consequently 0-104 m vertical integrals and fluxes at 104 m are
197 presented below. These summarize the euphotic zone results, where mesoscale
198 biological responses are most pronounced. In the simulations, small phytoplankton and
199 diatoms have little biomass below 104 m, such that deeper vertical integrals of their
200 biomass or primary production are very similar.

201 Standard errors presented below were computed by dividing the standard
202 deviations (computed from 100 five-day averages) by the square root of the number of
203 “independent observations”. For this we use the number of independent eddies as

204 determined by eddy tracking, which for Run 1 is 45 C, 40 A, 32 M and 19 T, and for Run
205 2 is 32 C, 29 A, 36 M and 28 T. Naturally, this approximately equals the total number of
206 eddies of each type counted in all 100 frames divided by the mean temporal correlation
207 timescale, which is approximately one month (6 frames). We also include in the standard
208 errors the uncertainty related to removing the large-scale spatial trend. This was done by
209 varying the spatial scales in the computation of the large-scale trend by ±20% (±33%
210 gave unacceptably poor separation of the large-scale trend from mesoscale anomalies),
211 and estimating this error as the mean difference of these cases from the standard case.
212 The detrending errors and eddy-variance errors were then combined.
213
214 3.1. Physical simulation results
215
216 As in previous studies (Zhai and Greatbach, 2007; Xu and Scott, 2008; Small et
217 al., 2009; Eden and Dietze, 2009), the standard deviation of sea level anomaly (SLA)
218 declined from Run 1 to Run 2 (Fig. 1). Comparison of Fig. 1b with the observation-
219 based estimates in Fig. 4a of Scharffenberg and Stammer (2010) show a significant
220 underestimation of sea level variability throughout the basin except for the Gulf Stream.
221 Nevertheless, both runs exhibit an energetic mesoscale environment, as evidenced by a
222 zoomed-in view of a subdomain in the Sargasso Sea (Fig. 2a,b). The correlation between
223 SLA and negative density anomaly at 729 m is very high, exceeding 0.94 in Run 1. Yet
224 density anomalies at 97 m show a greater amount of submesoscale variance, and often
225 occur at the edges of eddies in both runs (Fig. 2c,d). The mean amplitude of SLA
226 perturbations at the center of all eddy types in the Sargasso Sea drops by about a factor of

two from Run 1 to Run 2 (Fig. 3a,b). This is the expected response, as eddy/wind interaction drives downwelling in cyclones and upwelling in anticyclones, and thus is a mechanism that accelerates eddy decay (Dewar and Flierl, 1987).

In Run 1 the highest amplitude isopycnal shoaling at 97 m is at the center of cyclones (Fig. 3c), whereas in Run 2 the density anomalies at the center of mode-water eddies and cyclones are comparable. Interestingly in both runs the isopycnals at eddy edges (150 km from eddy center) are on average displaced above the local mean. Examples of this can be seen in Fig. 2c,d where positive density anomalies (red) frequently lie on top of the zero SLA lines. In Run 2, the mean density anomalies at the edges of cyclones and thinnies rival the magnitude of the density anomaly at cyclone centers (Fig. 3d). During the EDDIES experiment, upward displaced isopycnals at eddy edges was sometimes seen (Fig. 3A in Ewart et al., 2008).

Note the error bars in Fig. 3 are standard errors, i.e. the uncertainty in the means, which are roughly 6 times smaller than the standard deviations. By multiplying the error bars in Fig. 3d by a factor of 6, one can see that the variability in radial structure is large, to the point that any individual eddy may not exhibit a clear radial pattern in density at 97 m (Fig. 2d). It is only after averaging over many eddies (400 days in a 5° by 10° domain) that the mean radial patterns emerge.

One would expect eddy/wind interaction to cause upwelling at the center of mode-water eddies and anticyclones and downwelling at the center of cyclones and thinnies. Although the vertical velocities are too variable to distinguish these trends, evidence for their integrated effect is suggested by the nitrate concentration anomalies at 104 m (Fig. 3e,f), which increase from Run 1 to Run 2 at the center of mode-water eddies

and anticyclones, and decrease at the center of cyclones, though thinnies change little. These nitrate anomalies at the base of the euphotic zone are modest compared with field observations in mode-water eddies of +0.3 μM at that depth (Table 2 in Li and Hansell, 2008). Also seen is enhanced nitrate at the edges of cyclones and thinnies, similar to and related to the displacements seen in density.

The eddy/wind interaction significantly changed the distribution of eddy types (Fig. 4a). The number of regular cyclones decreased and the number of thinnies increased, both by a factor of two. The number of mode-water eddies increased by 17%, though surprisingly the number of regular anticyclones did not change significantly. Observations from the EDDIES cruises provide a means to assess these simulated eddy demographics, although the total number of eddies sampled was relatively small. During EDDIES, 3 of 5 anticyclones investigated turned out to be mode-water eddies, statistically indistinguishable from the 48% and 52% of Run 1 and Run 2. During EDDIES, 1 of 5 cyclones transformed from a cyclone into a thinny during the period of observation, closer to Run 1 (in which 28% of all cyclones are thinnies) than Run 2 (64%). The simulations can also be compared with satellite SLA observations, although the satellite altimetry alone cannot distinguish regular cyclones from thinnies nor regular anticyclones from mode-water eddies, such that comparison can only be made regarding all cyclones (C + T) and all anticyclones (A + M). The AVISO sea level anomaly gridded data were analyzed in the same manner as the model: 5-day averages were retrieved in the Sargasso subdomain between year days 150-275 (for years 2006-2009, as before 2006 only 3.5-day analyses are available), and the large-scale spatial trend removed. The number of cyclones and anticyclones in the Sargasso Sea is greater in the

observations than in the model, though Run 2 is an improvement over Run 1 (Fig. 4b). SLA amplitude for both cyclones and anticyclones is overestimated in Run 1 (Fig. 4c), while inclusion of eddy-wind interaction decreases SLA amplitudes of both cyclones and anticyclones to below the AVISO estimates. Note the AVISO analysis is performed on a 0.33° longitude grid, and smoothing of the data by objective analysis onto a grid of that resolution may cause underestimation of eddy amplitudes. Thus it is likely the true SLA amplitudes are closer to those of Run 1 than Run 2. Previous POP 0.1° North Atlantic simulations without eddy/wind interaction have generally shown good agreement with various data types (Smith et al., 2000; McClean et al., 2002; Tokmakian and McClean, 2003; Brachet et al., 2004). Comparison with satellite-based maps of eddy kinetic energy (EKE) (Stammer et al., 2006) also reveal that Run 1 is in better agreement with observations than Run 2.

3.2. Biological simulation results

Spatial structure in the biomass anomalies for all phytoplankton groups tend to correlate positively with density anomalies at 97 m (Fig. 5). As expected, biomass is highest where isopycnal displacements are upward, in response to enhanced specific growth rates, which are due to local uplift of the nitracline and phosphocline (Fig. 3e,f) to higher light intensities.

Phytoplankton biomass and growth rate anomalies show systematic variations as a function of eddy type and distance from eddy center (Figs. 6 and 7). In both runs, biomass and growth rate anomalies are highest at the center of mode-water eddies,

296 followed by cyclones, then generally anticyclones followed by thinnies. Biomass and
297 growth rate anomalies are also significantly positive at the outer edges of cyclones and
298 thinnies, which has at times been observed (Ewart et al., 2008; Mourino-Carballido,
299 2009). Including the eddy/wind interaction significantly increases the diatom growth rate
300 and biomass anomalies at the center of mode-water eddies, increases small phytoplankton
301 and diazotroph anomalies at the center of cyclones from negative to positive, and
302 increases the anomalies at the edges of cyclones and thinnies. The EDDIES cruises did
303 find higher Chl (and in particular diatoms) in mode-water eddies than in cyclones. Thus
304 the eddy/wind interaction brings the simulation into better agreement with observations
305 of mesoscale variations in phytoplankton community composition. Neither run, however,
306 reproduced the observed correlation between diazotrophs and anticyclones (see Sec. 4).
307 Another way to visualize the model results which includes all grid points, not just
308 eddies, is to bin properties according to SLA and density anomaly at 97 m, separating the
309 four eddy types into four quadrants (Figs. 8-9). The first obvious difference is that the
310 ranges of both SLA and density anomalies in Run 2 are about half those of Run 1. The
311 range and variance of density anomalies at 100 m observed at BATS is actually closer to
312 Run 2 than Run 1 (not shown). Regarding biomass anomalies (Fig. 8), Run 2 shows
313 positive phytoplankton biomass anomalies in mode-water eddies and cyclones, and
314 negative anomalies in anticyclones and thinnies. The relationship is primarily a function
315 of density anomaly rather than SLA. The highest biomass anomalies are for diatoms,
316 which is qualitatively consistent with observations; however, the magnitude of the
317 anomalies is still lower than observed (McGillicuddy et al., 2007). The background
318 shading in Fig. 8 shows the general tendency of field data, discussed below (Sec. 4).

Highest growth rate anomalies for all phytoplankton species are found in mode-water eddies and cyclones, up to +28% to +39%, again in response to near-surface isopycnal displacements (Fig. 9) bringing nutrients into higher light intensities.

4. Discussion

Run 2 (with eddy/wind interaction) better represents some basic aspects of observed mesoscale perturbations to phytoplankton species composition. Both Run 2 and observations agree on the strongest biological response being that of diatoms at the center of mode-water eddies, followed by small phytoplankton in mode-water eddies and cyclones. While neither run suggests a significant mean enhancement in diatoms at the center of cyclones (Fig. 6e,f), enhanced diatoms do occur in some cyclones (Fig. 8), often as submesoscale azimuthal variability. This has not been observed in the Sargasso Sea, though it has in cyclones off Hawaii during eddy formation (Benitez-Nelson et al., 2007). As the sampling during the EDDIES cruises was limited to mature eddies, this type of ephemeral diatom bloom in forming cyclones may have been missed (Benitez-Nelson and McGillicuddy, 2008). Accordingly, the background shading of the C quadrants in Fig. 8 has been left blank to reflect this uncertainty. Two EDDIES cyclones did show relatively low silicate concentrations at their centers, which may be indicative of prior diatom blooms (Li and Hansell, 2008). Alternatively Bibby and Moore (submitted) have suggested the lack of diatom blooms in Sargasso Sea cyclones results from differences in silicate and nitrate concentrations of the upwelled water.

One clear discrepancy between simulated and observed species composition is that the model failed to reproduce the observed correlation of positive diazotroph biomass anomalies with anticyclones over cyclones. The reason may be related to any number of processes missing from the model. For example, *Trichodesmium* have gas vacuoles that allow them to be positively buoyant, potentially causing aggregation in regions of surface convergence. Such circumstances would be expected to occur during the genesis of anticyclones and throughout the lifetimes of thinnies and cyclones. The model diazotrophs, in contrast, currently have neutral buoyancy. Secondly, it has been recently discovered that *Trichodesmium* can utilize DOP (Dyhrman et al., 2006; Orchard et al., 2010). Preliminary simulations at 1.6° resolution show that this allows diazotrophs in the model to have highest biomass at the sea surface (in better agreement with observations), and should liberate their phosphorus-limited growth rates from association with cyclones and mode-water eddies. Thirdly, the temperature-dependence of their growth rate is actually much stronger than currently used in the model (Breitbarth et al., 2007). Finally, the enhancement of diazotroph in anticyclones could reflect eddy-driven horizontal advection across a large-scale gradient. The simulated annual mean diazotroph meridional gradient between 22 and 30 °N along 60-68 °W is only 5%, much smaller than the observed factor of two (Carpenter and Price, 1977; Carpenter and Romans, 1991). Therefore this possibility cannot be evaluated with the present model.

While the inclusion of eddy/wind interactions improved phytoplankton community structure (Figs. 6-9) and some aspects of eddy demographics (Fig. 4b), it degraded EKE (Fig. 1; cf. Sharffenberg and Stammer, 2010) and the magnitude of eddy SLA (Fig. 4c). An unrealistically weak eddy field potentially compromises both the

364 physical and biological aspects of the simulation, so it is of interest to increase SLA
365 variance back to observed levels. One possible way to increase EKE might be to
366 decrease horizontal viscosity. The viscosity scheme we used was calibrated largely based
367 on Gulf Stream separation (Plate 1 in Hecht et al., 2008); our Fig. 1 shows that the
368 eddy/wind interaction does reduce spurious SLA variability to the southeast of Cape
369 Hatteras, such that a further decrease in viscosity may be possible. However it is not
370 clear if the viscosity can be decreased at this grid resolution without degrading other
371 aspects of the physical simulation (Bryan et al., 2007), including increased numerical
372 noise (Jochum et al., 2008) to which vertical velocities and consequently biological
373 processes may be sensitive. If this does not prove successful, increased horizontal grid
374 resolution probably will be required. While 0.1° resolution adequately resolves
375 mesoscale eddies, it poorly resolves submesoscale processes that interact strongly with
376 the mesoscale. Bryan et al. (2007) note that the 0.1° North Atlantic POP simulation's
377 sensitivity to subgridscale parameterizations suggests the flow field is not yet at
378 convergence. Hurlburt and Hogan (2000) found convergence of physical eddy statistics
379 at approximately 0.03° resolution. We therefore anticipate a doubling or tripling of grid
380 resolution would bring the eddy intensities back to the observed levels. This higher grid
381 resolution should also improve the simulated nutrient fluxes and biological productivity
382 associated with submesoscale processes at the edges of eddies, although even 0.03°
383 resolution may not be sufficient for convergence of biological production (e.g., Levy et
384 al., 2001).

385 Similar to Eden and Dietze (2009), new production in the Sargasso subdomain
386 decreased slightly (13%) from Run 1 to Run 2. However because the eddy intensities in

Run 2 are lower than observed by roughly a factor of two, the eddy/wind interaction-driven vertical velocities are likely also underestimated by a factor of two. Consequently it is premature to assess the net impact of eddy/wind interaction on biological processes without first bringing the physical simulation into closer agreement with observations.

5. Conclusions

Including the eddy/wind interaction significantly changed the simulated physical properties of eddies in the Sargasso Sea, including the relative number of different types of eddies. This change in model forcing gave closer agreement with observations regarding the total number of eddies, and the range of density anomalies at 97 m. The simulation with eddy/wind interaction also yielded similar isopycnal displacements and nitrate concentrations at the centers of mode-water eddies and cyclones. However EKE and SLA variance became lower than observed, and the proportion of thinnies to regular cyclones became higher than observed. Decreased horizontal viscosity or increased horizontal grid resolution appears necessary to restore the model EKE back toward observations, which is a prerequisite to assessing the full impact of eddy/wind interaction on physical and biological processes in the North Atlantic.

Including the eddy/wind interaction brings the biological simulation into closer phenomenological agreement with observed eddy-phytoplankton relationships, viz. significantly enhanced diatom biomass and growth rates in mode-water eddies, and slightly enhanced small phytoplankton biomass in mode-water eddies and cyclones. The simulation suggests *in situ* growth as being the primary cause of enhanced phytoplankton

biomass found in cyclones and mode-water eddies, resulting from upward isopycnal displacements and elevated nutrients at the base of the euphotic zone. In contrast, the simulations did not reproduce enhanced diazotroph biomass in anticyclones, indicating that one or more processes are missing from the diazotroph parameterization.

Acknowledgements

We would like to thank Marjy Friedrichs for providing the Regional Testbed code, Jeff Dusenberry for implementation of the BEC model into the Regional Testbed, and Valery Kosnyrev for retrieval of the AVISO data. The simulations were run on the supercomputer Pleiades at NASA Ames Research Center using 512 parallel cores. LAA and DJM gratefully acknowledge the support of NASA grant 07-CARBON07-17. SCD and IDL gratefully acknowledge support from the NSF Center for Microbial Oceanography, Research and Education (C-MORE; NSF EF-0424599).

425 References

426

427 Barnier, B., Siefridt, L. and Marchesiello, P., 1995. Thermal forcing for a global ocean
428 circulation model using a three-year climatology of ECMWF analyses. Journal of
429 Marine Systems, 6: 363-380.
430 Benitez-Nelson, C.R., Bidigare, R.R., Dickey, T.D., Landry, M.R., Leonard, C.L.,
431 Brown, S.L., Nencioli, F., Rii, Y.M., Maiti, K., Becker, J.W., Bibby, T.S., Black,
432 W., Cai, W.J., Carlson, C.A., Chen, F.Z., Kuwahara, V.S., Mahaffey, C.,
433 McAndrew, P.M., Quay, P.D., Rappe, M.S., Selph, K.E., Simmons, M.P., Yang,
434 E.J., 2007. Mesoscale eddies drive increased silica export in the subtropical
435 Pacific Ocean. Science, 316(5827): 1017-1021.
436 Benitez-Nelson, C.R. and McGillicuddy, D.J., 2008. Mesoscale physical-biological-
437 biogeochemical linkages in the open ocean: An introduction to the results of the
438 E-FLUX and EDDIES programs. Deep-Sea Research II, 55(10-13): 1133-1138.
439 Bibby, T.S. and Moore, C.M., submitted. Silicate:nitrate ratios of upwelled waters
440 control the phytoplankton community sustained by mesoscale eddies in sub-
441 tropical North Atlantic and Pacific. Biogeosciences Discussions, 7:7505-7525.
442 Boyer, T.P., Stephens, C., Antonov, J.I., Conkright, M.E., Locarnini, R.A., O'Brien,
443 T.D., and Garcia, H.E., 2002. World Ocean Atlas 2001, Volume 2: Salinity. S.
444 Levitus, Ed., NOAA Atlas NESDIS 50, U.S. Government Printing Office,
445 Washington, D.C., 165 pp.

446 Brachet, S.P., Le Traon, P.Y. and Le Provost, C., 2004. Mesoscale variability from a
447 high-resolution model and from altimeter data in the North Atlantic Ocean.
448 Journal of Geophysical Research - Oceans, 109C, C12025.
449 Breitbarth, E., Oschlies, A. and LaRoche, J., 2007. Physiological constraints on the
450 global distribution of *Trichodesmium* --- effect of temperature on diazotrophy.
451 Biogeosciences, 4: 53-61.
452 Bryan, F.O., Hecht, M.W., and Smith, R.D., 2007. Resolution convergence and
453 sensitivity studies with North Atlantic circulation models. Part I: The western
454 boundary current system. Ocean Modelling, 16: 141-159.
455 Carpenter, E.J. and Price, C.C., 1977. Nitrogen fixation, distribution, and production of
456 *Oscillatoria* (*Trichodesmium*) spp. in the western Sargasso and Caribbean Seas.
457 Limnology and Oceanography, 22: 60-72.
458 Carpenter, E.J. and Romans, K., 1991. Major role of the cyanobacterium *Trichodesmium*
459 in nutrient cycling in the North Atlantic Ocean. Science, 254: 1356-1358.
460 Conkright, M.E., Garcia, H.E., O'Brien, T.D., Locarnini, R.A., Boyer, T.P., Stephens, C.,
461 and Antonov, J.I., 2002. World Ocean Atlas 2001, Volume 4: Nutrients. S.
462 Levitus, Ed., NOAA Atlas NESDIS 52, U.S. Government Printing Office,
463 Washington, D.C., 392 pp.
464 Davis, C.S. and McGillicuddy, D.J., 2006. Transatlantic Abundance of the N_2-Fixing
465 Colonial Cyanobacterium *Trichodesmium*. Science, 312: 1517-1520.
466 Dewar, W.K. and Flierl, G.R., 1987. Some effects of wind on rings. Journal of Physical
467 Oceanography, 17: 1653-1667.

468 Ducklow, H.W., and Harris, R.P., 1993. Introduction to the JGOFS North Atlantic Bloom
469 Experiment. Deep-Sea Reasearch II, 40(1-2): 1-8.
470 Dyhrman, S.T., Chappell, P.D., Haley, S.T., Moffett, J.W., Orchard, E.D., Waterbury,
471 J.B. and Webb, E.A., 2006. Phosphonate utilization by the globally important
472 marine diazotroph *Trichodesmium*. Nature, 439(7072): 68-71.
473 Eden, C. and Dietze, H., 2009. Effects of mesoscale eddy/wind interactions on biological
474 new production and eddy kinetic energy. Journal of Geophysical Research -
475 Oceans, 114(C5), C05023.
476 Ewart, C.S., Meyers, M.K., Wallner, E.R., McGillicuddy, D.J. and Carlson, C.A., 2008.
477 Microbial dynamics in cyclonic and anticyclonic mode-water eddies in the
478 northwestern Sargasso Sea. Deep-Sea Research II, 55(10-13): 1334-1347.
479 Friedrichs, M.A.M., Dusenberry, J.A., Anderson, L.A., Armstrong, R.A., Chai, F.,
480 Christian, J.R., Doney, S.C., Dunne, J., Fujii, M., Hood, R., McGillicuddy, D.J.,
481 Moore, J.K., Schartau, M., Spitz, Y.H. and Wiggert, J.D., 2007. Assessment of
482 skill and portability in regional marine biogeochemical models: Role of multiple
483 planktonic groups. Journal of Geophysical Research - Oceans, 112(C8), C08001.
484 Garcia, H.E., Locarnini, R.A., Boyer, T.P. and Antonov, J.I., 2006a. World Ocean Atlas
485 2005, Volume 3: Dissolved Oxygen, Apparent Oxygen Utilization, and Oxygen
486 Saturation. S. Levitus, Ed. NOAA Atlas NESDIS 63, U.S. Government Printing
487 Office, Washington, D.C, 342 pp.
488 Garcia, H.E., Locarnini, R.A., Boyer, T.P. and Antonov, J.I., 2006b. World Ocean Atlas
489 2005, Volume 4: Nutrients (phosphate, nitrate, silicate). . Levitus, Ed. NOAA
490 Atlas NESDIS 64, U.S. Government Printing Office, Washington, D.C, 396 pp.

491 Hecht, M.W., Petersen, M.R., Wingate, B.A., Hunke, E. and Maltrud, M., 2008. Lateral
492 mixing in the eddying regime and a new broad-ranging formulation. In: Hecht,
493 M.W., Hasumi, H. (Eds.), Ocean Modeling in an Eddying Regime, Geophysical
494 Monograph Series 177, American Geophysical Union, Washington, D.C., pp.
495 339-352.
496 Hurlburt, H.E. and Hogan, P.J., 2000. Impact of 1/8° to 1/64° resolution on Gulf Stream
497 model-data comparisons in basin-scale subtropical Atlantic Ocean models.
498 Dynamics of Atmospheres and Oceans, 32: 283-329.
499 Jochum, M., Danabasoglu, G., Holland, M., Kwon, Y.-O. and Large, W.G., 2008. Ocean
500 viscosity and climate. Journal of Geophysical Research - Oceans, 113C, C06017.
501 Key, R.M., Kozyr, A., Sabine, C.L., Lee, K., Wanninkhof, R., Bullister, J.L., Feeley,
502 R.A., Millero, F.J., Mordy, C. and Peng, T.-H., 2004. A global ocean carbon
503 climatology: Results from Global Data Analysis Project (GLODAP). Global
504 Biogeochemical Cycles, 18, GB4031.
505 Krause, J.W., Nelson, D.M. and Lomas, M.W., 2010. Production, dissolution,
506 accumulation, and potential export of biogenic silica in a Sargasso Sea mode-
507 water eddy, Limnology and Oceanography, 55:569-579.
508 Large, W.G., McWilliams, J.C. and Doney, S.C., 1994. Oceanic vertical mixing: A
509 review and a model with a nonlocal boundary layer parameterization. Reviews of
510 Geophysics, 32: 363-403.
511 Large, W.G. and Pond, S., 1981. Open ocean momentum flux measurements in moderate
512 to strong winds. Journal of Physical Oceanography, 11: 324-336.

513 Large, W.G. and Pond, S., 1982. Sensible and latent heat flux measurements over the
514 ocean. Journal of Physical Oceanography, 12: 464-482.
515 Large, W.G. and Yeager, S.G., 2004. Diurnal to decadal global forcing for ocean and sea-
516 ice models: The data sets and flux climatologies. NCAR Technical Note
517 NCAR/TN-460+STR, Climate and Global Dynamics Division, National Center
518 for Atmospheric Research, Boulder, CO.
519 Ledwell, J.R., McGillicuddy, D.J. and Anderson, L.A., 2008. Nutrient flux into an intense
520 deep chlorophyll layer in a mode-water eddy. Deep Sea Research II, 55(10-13):
521 1139-1160.
522 Lévy, M., Klein, P. and Treguier, A.-M., 2001. Impact of sub-mesoscale physics on
523 production and subduction of phytoplankton in an oligotrophic regime. Journal of
524 Marine Research, 59(4): 535-565.
525 Li, Q.P. and Hansell, D.A., 2008. Nutrient distributions in baroclinic eddies of the
526 oligotrophic North Atlantic and inferred impacts on biology. Deep-Sea Research
527 II, 55(10-13): 1291-1299.
528 Locarnini, R.A., O'Brien, T.D., Garcia, H.E., Antonov, J.I., Boyer, T.P., Conkright,
529 M.E., and Stephens, C., 2002. World Ocean Atlas 2001, Volume 3: Oxygen. S.
530 Levitus, Ed., NOAA Atlas NESDIS 51, U.S. Government Printing Office,
531 Washington, D.C., 286 pp.
532 Martin, A.P. and Richards, K.J., 2001. Mechanisms for vertical nutrient transport within a
533 North Atlantic mesoscale eddy. Deep-Sea Research II, 48: 757-773.

McClean, J.L., Poulain, P.-M., Pelton, J.W. and Maltrud, M.E., 2002. Eulerian and Lagrangian statistics from surface drifters and a high-resolution POP simulation in the North Atlantic, Journal of Physical Oceanography, 32, 2472-2491.

McGillicuddy, D.J., Anderson, L.A., Doney, S.C. and Maltrud, M.E., 2003. Eddy-driven sources and sinks of nutrients in the upper ocean: results from a 0.1 degree resolution model of the North Atlantic. Global Biogeochemical Cycles, 17(2), 1035, doi:10.1029/2002GB001987.

McGillicuddy, D.J., Anderson, L.A., Bates, N.R., Bibby, T., Buesseler, K.O., Carlson, C.A., Davis, C.S., Ewart, C., Falkowski, P.G., Goldthwait, S.A., Hansell, D.A., Jenkins, W.J., Johnson, R., Kosnyrev, V.K., Ledwell, J.R., Li, Q.P., Siegel, D.A.S. and Steinberg, D.K., 2007. Eddy/wind interactions stimulate extraordinary mid-ocean plankton blooms. Science, 316: 1021-1026.

McGillicuddy, D.J., Johnson, R., Siegel, D.A., Michaels, A.F., Bates, N.R. and Knap, A.H., 1999. Mesoscale variations of biogeochemical properties in the Sargasso Sea. Journal of Geophysical Research - Oceans, 104(C6): 13,381-13,394.

Moore, J.K., Doney, S.C. and Lindsay, K., 2004. Upper ocean ecosystem dynamics and iron cycling in a global three-dimensional model. Global Biogeochemical Cycles, 18, GB4028.

Moore, J.K., Doney, S.C., Lindsay, K., Mahowald, N. and Michaels, A.F., 2006. Nitrogen fixation amplifies the ocean biogeochemical response to decadal timescale variations in mineral dust deposition. Tellus, 58B: 560-572.

555 Moore, J.K. and Doney, S.C., 2007. Iron availability limits the ocean nitrogen inventory
556 stabilizing feedbacks between marine denitrification and nitrogen fixation. Global
557 Biogeochemical Cycles, 21(2), GB2001.
558 Mouriño-Carballido, B., 2009. Eddy-driven pulses of respiration in the Sargasso Sea.
559 Deep-Sea Research I, 56(8): 1242-1250.
560 Orchard, E.D., Ammerman, J.W., Lomas, M.W., and Dyhrman, S.T., 2010. Dissolved
561 inorganic and organic phosphorus uptake in *Trichodesmium* and the microbial
562 community: The importance of phosphorus ester in the Sargasso Sea. Limnology
563 and Oceanography, 55: 1390-1399.
564 Oschlies, A. and Garcon, V., 1999. An eddy-permitting coupled physical-biological
565 model of the North Atlantic. 1. Sensitivity to physics and numerics. Global
566 Biogeochemical Cycles, 13: 135-160.
567 Pacanowski, R.C. and Philander, S.G.H., 1981. Parameterization of vertical mixing in
568 numerical models of the tropical oceans. Journal of Physical Oceanography, 11:
569 1443-1451.
570 Scharffenberg, M.G., and Stammer, D., 2010. Seasonal variations of the large-scale
571 geostrophic flow field and eddy kinetic energy inferred from the
572 TOPEX/Poseidon and Jason-1 tandem mission data. Journal of Geophysical
573 Research - Oceans, 115(C), C02008.
574 Small, R.J., Richards, K.J., Xie, S.-P., Dutrieux, P. and Miyama, T., 2009. Damping of
575 Tropical Instability Waves caused by the action of surface currents on stress,
576 Journal of Geophysical Research – Oceans, 114, C04009.

577 Smith, R.D., Dukowicz, J.K., and Malone, R.C., 1992. Parallel ocean circulation
578 modeling. Physica D, 60: 38-61.
579 Smith, R., Maltrud, M., Bryan, F. and Hecht, M., 2000. Numerical simulation of the
580 North Atlantic Ocean at 1/10°. Journal of Physical Oceanography, 30: 1532-1561.
581 Stammer, D., Wunsch, C. and Ueyoshi, K., 2006. Temporal changes in ocean eddy
582 transports. Journal of Physical Oceanography, 36: 543-550.
583 Steinberg, D.K., Carlson, C.A., Bates, N.R., Johnson, R.J., Michaels, A.F. and Knap,
584 A.H., 2001. Overview of the US JGOFS Bermuda Atlantic Time-series Study
585 (BATS): a decade-scale look at ocean biology and biogeochemistry. Deep-Sea
586 Research II, 48(8-9): 1405-1447.
587 Stephens, C., Antonov, J.I., Boyer, T.P., Conkright, M.E., Locarnini, R.A., O'Brien,
588 T.D., and Garcia, H.E., 2002. World Ocean Atlas 2001, Volume 1: Temperature.
589 S. Levitus, Ed., NOAA Atlas NESDIS 49, U.S. Government Printing Office,
590 Washington, D.C., 167 pp.
591 Sweeney, E.N., McGillicuddy, D.J. and Buesseler, K.O., 2003. Biogeochemical impacts
592 due to mesoscale eddy activity in the Sargasso Sea as measured at the Bermuda
593 Atlantic Time Series (BATS) site. Deep-Sea Research II, 50: 3017-3039.
594 Tokmakian, R. and McClean, J.L., 2003. How realistic is the high frequency signal of a
595 0.1° resolution ocean model?, Journal of Geophysical Reasearch - Oceans,
596 108(C4), 3115.
597 Xu, Y. and Scott, R.B., 2008. Subtleties in forcing eddy resolving ocean models with
598 satellite wind data. Ocean Modelling, 20(3): 240-251.

599 Zhai, X. and Greatbatch, R.J., 2007. Wind work in a model of the northwest Atlantic
600 Ocean. Geophysical Research Letters, 34, L04606.
601

602 Captions

603

604 Fig. 1. Standard deviation of sea level anomaly (SLA) in (a) Run 1 (no eddy/wind
605 interaction), and (b) Run 2 (with eddy/wind interaction). The white box is the Sargasso
606 Sea subdomain. In this figure only, SLA is computed as the anomaly from the 4-year
607 temporal mean, to compare directly with fig. 4a of Scharffenberg and Stammer (2010).

608

609 Fig. 2. (a) Run 1 (no eddy/wind interaction) and (b) Run 2 (with eddy/wind interaction)
610 sea level anomaly for the final 5-day average of each run (year 21, day 190-195). SLA is
611 defined as sea surface height with the large-scale spatial trend removed. The thick black
612 line is zero, dashed lines are negative, and the contour interval is 3 cm. (c) Run 1 and (d)
613 Run 2 in situ density anomalies (kg m^{-3}) at 97 m. SLA contours from (a) and (b) are
614 overlain in black, with eddy types identified based on SLA and density anomaly (C =
615 regular cyclone, A = regular anticyclone, M = mode-water eddy, T = thinny).

616

617 Fig. 3. Mean properties with standard errors of regular cyclones (black), regular
618 anticyclones (red), mode-water eddies (green) and thinnies (blue), as a function of
619 distance from eddy centers, in the Sargasso Sea subdomain for Run 1 (no eddy/wind
620 interaction, left column) and Run 2 (with eddy/wind interaction, right column). The top
621 row shows sea level anomalies. The middle row shows in situ density anomalies at 97 m.
622 The bottom row shows nitrate concentration anomalies at 104 m. From each 5-day
623 average, anomaly fields are computed by removing the large-scale 2-D horizontal trends,
624 locating the eddy centers, and aggregating values in the surrounding points into 10-km

625 radial bins. For each of these bins, means and standard deviations are computed. The
626 estimation of standard errors is described in the fourth paragraph of Sec. 3.
627
628 Fig. 4. (a) Mean number of eddies in the Sargasso Sea subdomain (25-30 °N, 68-58 °W,
629 from 100 frames, viz. 5-day averages from year day 150-275 of 4 simulated years)
630 classified based on SLA and density anomaly at 97 m, for Run 1 ("R1", no eddy/wind
631 interaction) and Run 2 ("R2", with eddy/wind interaction). C = regular cyclone, A =
632 regular anticyclone, M = mode-water eddy, T = thinny. The estimation of standard errors
633 is described in the fourth paragraph of Sec. 3. (b) Mean number of cyclones and
634 anticyclones compared with an observation-based estimate ("Obs") from the 2006-2009
635 AVISO altimetry data. (c) Mean magnitude of sea level anomaly of cyclones and
636 anticyclones compared with 2006-2009 AVISO altimetry data ("Obs").
637
638 Fig. 5. Run 2 0-104 m vertically-integrated phytoplankton biomass (mg C m^{-2})
639 anomalies, expressed as percent anomaly from large-scale means, for (a) small
640 phytoplankton, (c) diatoms and (e) diazotrophs, for year 21 day 190-195. In situ density
641 anomalies at 97 m (from Fig. 2d) are contoured in black, the thick line being zero, dashed
642 lines negative and the contour interval 0.1 kg m^{-3}. Panels (b), (d) and (f) show
643 corresponding specific growth rates (d^{-1}), computed as 0-104 m primary production rates
644 (mg C m^{-2} d^{-1}) divided by 0-104 m biomass (mg C m^{-2}), and expressed as percent
645 anomaly from large-scale mean growth rates, with density anomalies contoured in black.
646 Note that positive biomass and growth rate anomalies for all species correlate with
647 positive density anomalies. Run 1 also shows phytoplankton biomass and growth rate

anomalies to be highly correlated with density anomalies. Run 2 is shown because its density anomalies and SLA are less correlated than in Run 1 (Fig. 2), showing the relationship is with density not SLA.

Fig. 6. 0-104 m vertically-integrated phytoplankton biomass (mg C m^{-2}) anomalies, expressed as percent anomaly from the large-scale means, with standard errors for regular cyclones (black), regular anticyclones (red), mode-water eddies (green) and thinnies (blue), as a function of distance from eddy centers, in the Sargasso Sea subdomain for Run 1 (no eddy/wind interaction, left column) and Run 2 (with eddy/wind interaction, right column). The top row shows total phytoplankton biomass anomalies; second row, small phytoplankton biomass anomalies; third row, diatom biomass anomalies; bottom row, diazotroph biomass anomalies. From each 5-day average, anomaly fields are computed by removing the large-scale 2-D horizontal trends, locating the eddy centers, and aggregating values in the surrounding points into 10-km radial bins. For each of these bins, means and standard deviations are computed. The estimation of standard errors is described in the fourth paragraph of Sec. 3.

Fig. 7. Specific growth rate anomalies with standard errors for regular cyclones (black), regular anticyclones (red), mode-water eddies (green) and thinnies (blue), as a function of distance from eddy centers, in the Sargasso Sea subdomain for Run 1 (no eddy/wind interaction, left column) and Run 2 (with eddy/wind interaction, right column). The top row shows total phytoplankton growth rate (d^{-1}) anomalies, computed as 0-104 m primary production rates (mg C m^{-2} d^{-1}) divided by 0-104 m biomass (mg C m^{-2}), and

671 expressed as percent anomaly from large-scale mean growth rates. The second row
672 shows small phytoplankton specific growth rate anomalies; third row, diatom specific
673 growth anomalies; bottom row, diazotroph specific growth rate anomalies. From each 5-
674 day average, anomaly fields are computed by removing the large-scale 2-D horizontal
675 trends, locating the eddy centers, and aggregating values in the surrounding points into
676 10-km radial bins. For each of these bins, means and standard deviations are computed.
677 The estimation of standard errors is described in the fourth paragraph of Sec. 3.
678
679 Fig. 8. Run 1 (no eddy/wind interaction, top row) and Run 2 (with eddy/wind interaction,
680 bottom row) 0-104 m phytoplankton biomass anomalies (mg C m^{-2}), expressed as percent
681 anomaly from the large-scale mean, binned according to SLA and in situ density anomaly
682 at 97 m in the Sargasso Sea subdomain. The first column shows total phytoplankton
683 biomass anomaly; second column, small phytoplankton biomass anomaly; third column,
684 diatom biomass anomaly; fourth column, diazotroph biomass anomaly. The four
685 quadrants correspond to anticyclones (A), mode-water eddies (M), thinnies (T) and
686 cyclones (C). The background shading indicates the tendency of Sargasso Sea field data
687 e.g. diatom biomass anomalies are generally observed to be positive in mode-water
688 eddies, negative in anticyclones and thinnies, with cyclones uncertain (see text, Sec. 4).
689 Darker background shading of diatoms in mode-water eddies is used to reflect the fact
690 that highest Chl anomalies have been observed in those features (Fig. 2A in
691 McGillicuddy et al., 2007).
692

693 Fig. 9. Run 1 (no eddy/wind interaction, top row) and Run 2 (with eddy/wind interaction,
694 bottom row) phytoplankton specific growth rate anomalies, binned according to in situ
695 density anomaly and SLA, in the Sargasso Sea subdomain. The first column shows total
696 phytoplankton specific growth rate (d^{-1}) anomalies, computed as 0-104 m primary
697 production rates (mg C m^{-2} d^{-1}) divided by 0-104 m biomass (mg C m^{-2}), and expressed
698 as percent anomaly from large-scale mean growth rates. The second column shows small
699 phytoplankton growth rate anomalies; third column, diatom growth rate anomalies; fourth
700 column, diazotroph growth rate anomalies. The four quadrants correspond to
701 anticyclones (A), mode-water eddies (M), thinnies (T) and cyclones (C).
702

703

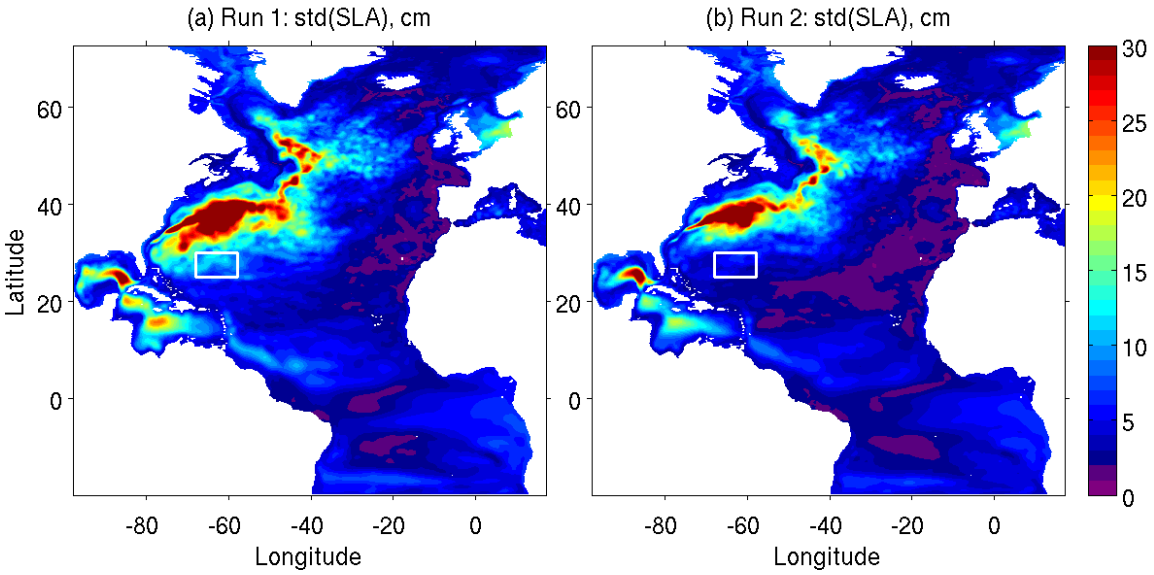

704

705 Fig. 1.

706

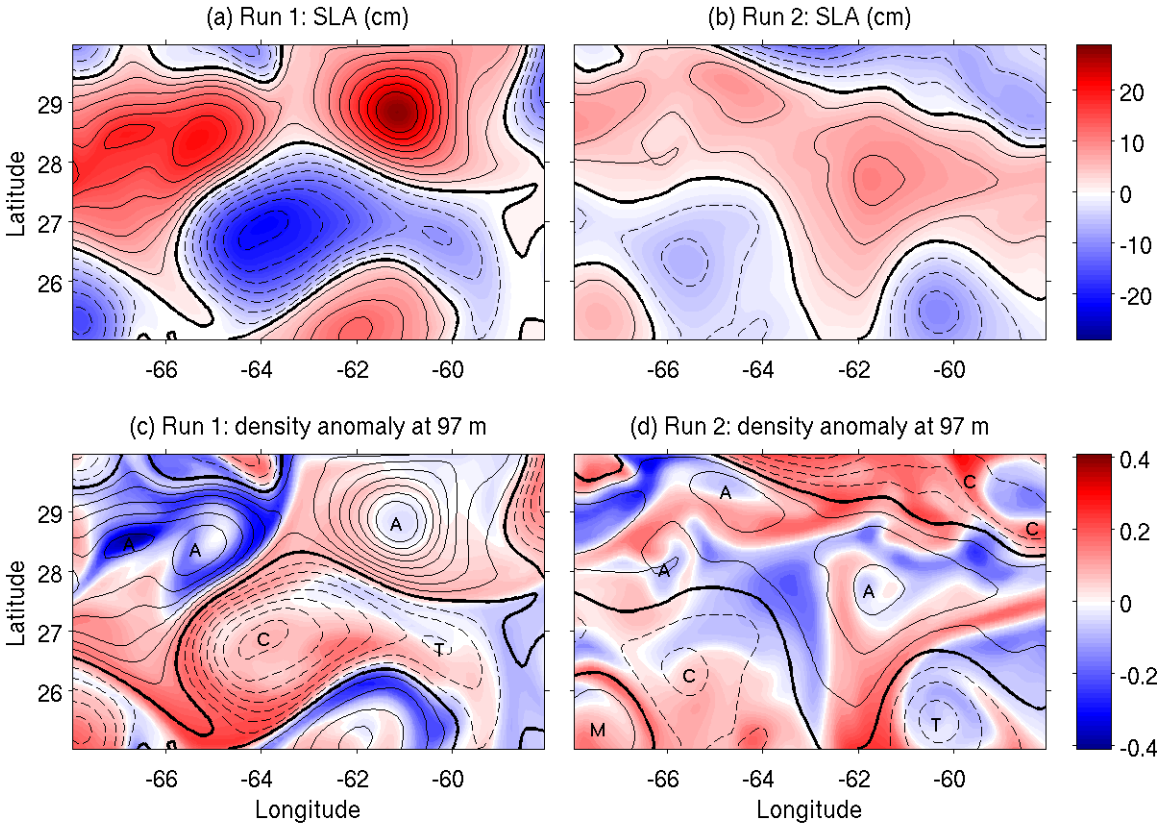

707

708

709 Fig. 2.

710

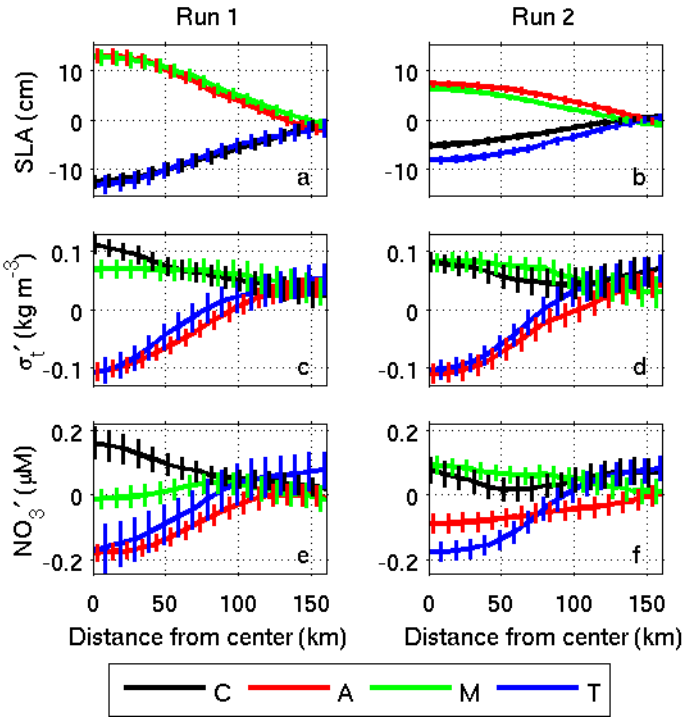

711

712

713 Fig. 3.

714

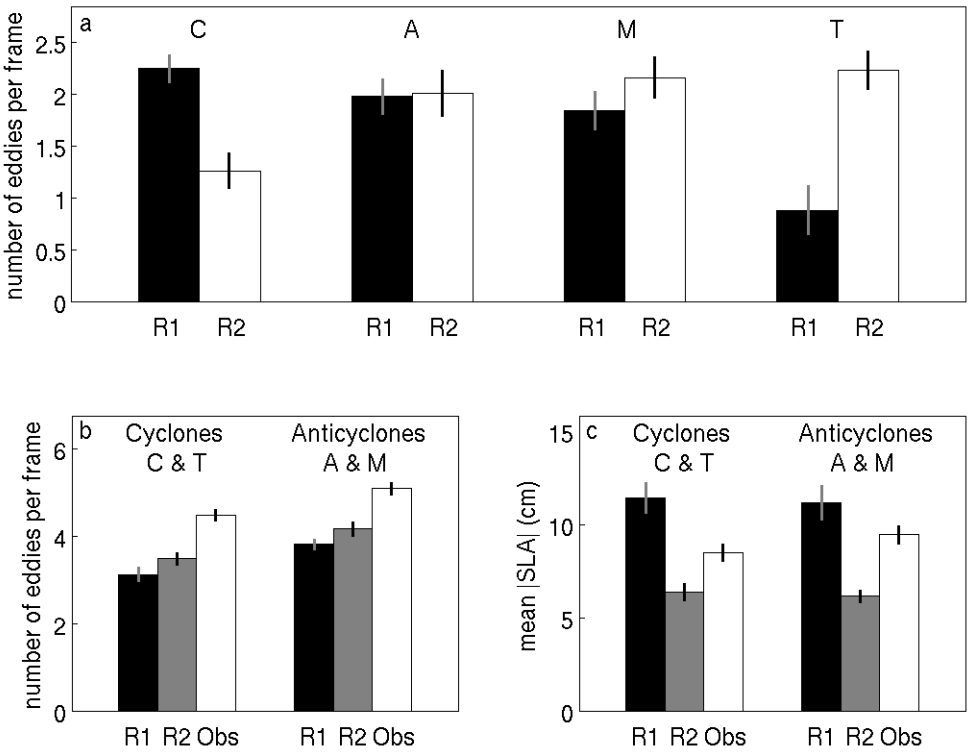
a
C
A
M
T
number of eddies per frame
2.5
2
1.5
1
0.5
0
R1
R2
b
Cyclones
C & T
Anticyclones
A & M
number of eddies per frame
6
4
2
0
R1 R2 Obs
c
mean |SLA| (cm)
15
10
5

715

716 Fig. 4.

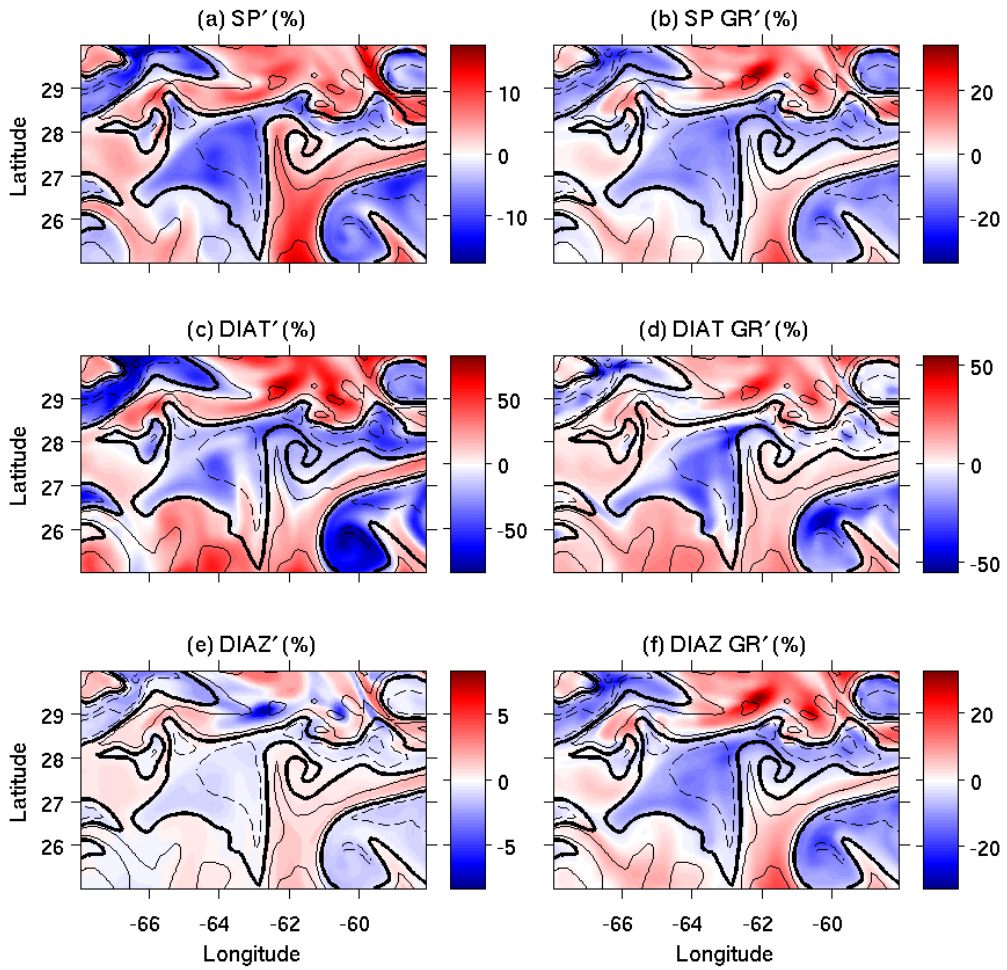

717

718 Fig. 5.

719

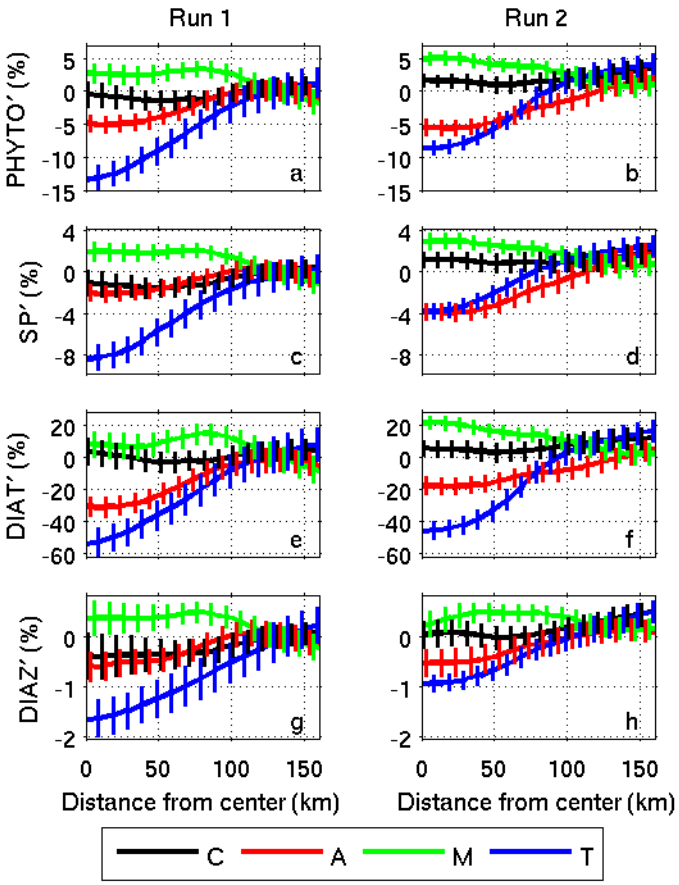

720

721 Fig. 6.

722

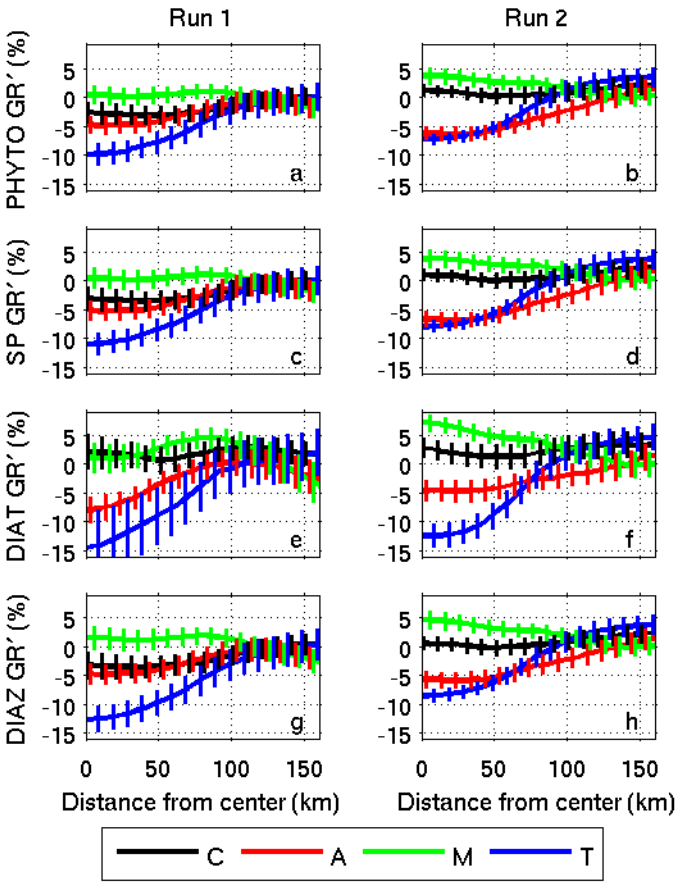

723

724 Fig. 7.

725

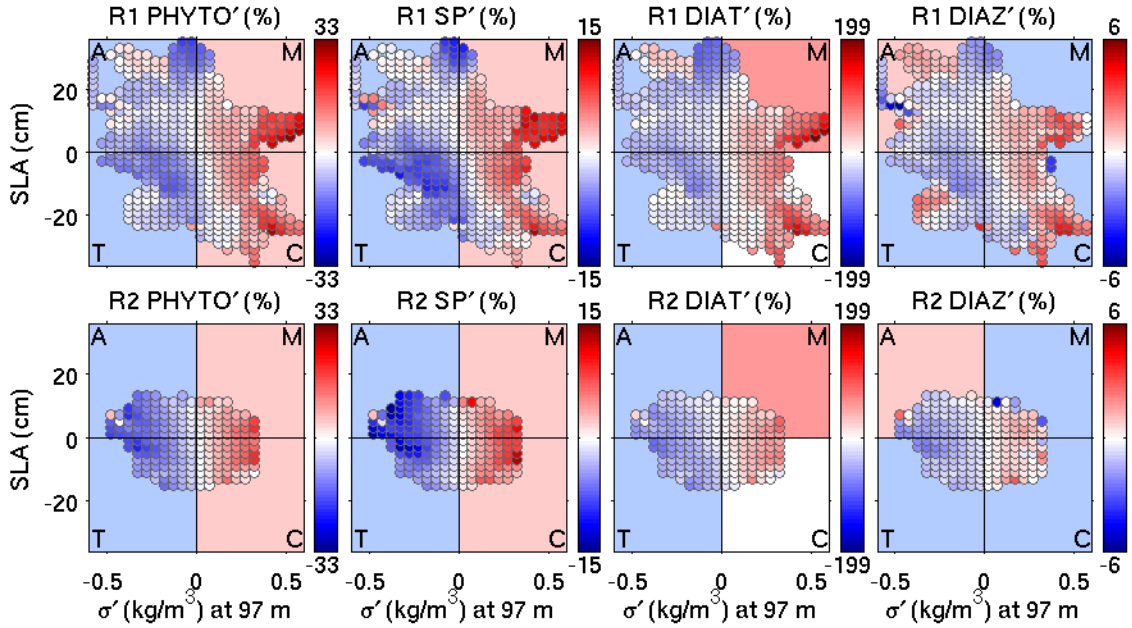

726

727

728 Fig. 8.

729

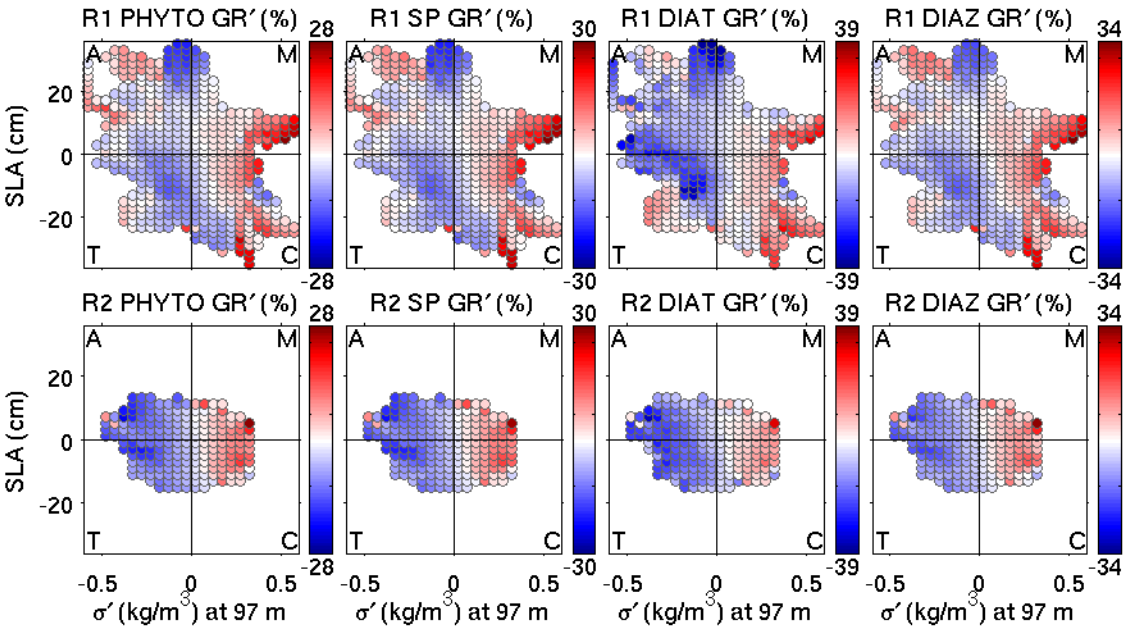

730

731

732 Fig. 9.